ANALYTICAL METHODS

Starting materials

The experiments were performed with either a mid-ocean ridge basalt (MORB) or a sample of the Central Atlantic Magmatic Province (CAMP), AN31, collected from a (Lower unit) lava flow in Morocco (table DR1). Samples were ground to less than 50 μm in size and stored in a drying oven before experiments. The AN31 was enriched in sulfur through the addition of pyrrhotite to create a bulk composition with 911 ppm S.

	SiO_2	TiO_2	Al_2O_3	FeO*	MnO	MgO	CaO	Na_2O	K_2O	P_2O_5	S (ppm)	Total
MORB	49.5	1.28	15.4	9.37	0.18	8.89	11.7	2.4	0.1	0.11	842	98.93
AN-31	50.2	1.17	11.1	11.4	0.18	12.8	9.07	1.63	0.66	0.12	911	98.33

Table DR1. Major element and S compositions for the two starting materials used for the experiments. Oxides concentrations are expressed as wt.%, S concentration as ppm. FeO*: total iron as FeO.

Crystallization experiments

The rock powders for experimental samples were placed inside graphite capsules, inserted into Pt outer capsules and dried in the oven before welding. The double capsule minimizes iron loss and creates oxygen fugacity conditions below the fayalite-quartz-magnetite buffer; at these conditions almost all sulfur dissolved in the melt is sulfide (S^{2-}; Jugo et al., 2010). Experiments were performed in a piston-cylinder using NaCl-pyrex-crushible alumina assemblies following the techniques of Baker (Baker, 2004). Experiments were simultaneously heated and pressurized to conditions above the liquidus and held at those conditions for 2 hours to ensure melt homogenization and destruction of any crystals in the starting material before cooling to subliquidus conditions where crystal growth occurred (Table DR2). Conditions were chosen to contain only a few crystals because reconnaissance experiments further below the liquidus demonstrated significant compositional heterogeneity in the pyroxenes at these conditions.

Run-product phases were analyzed for major elements on the electron microprobe using glass and mineral standards following the technique of Liu et al. (2007). In particular, basaltic glass standards VG-2 (1410 ppm S) and VG-A99 (125 ppm S) were repeatedly analyzed to ensure the accuracy of our analyses. The average major element compositions of the crystals are given in terms of their end-member components in Table DR2 and the average compositions of glasses are provided in Table DR3.

Experiment	Material	Pressure Gpa	Temperature °C	Time h	Phase assemblage and compositions Wo,En,Fs; Fo; An
2012-29	AN-31	0.8	1350/1240	2.0/21.2	glass, Low-Ca px: $Wo_4En_{83}Fs_{13}$; Oliv: Fo_{85}
2012-35	AN-31	1	1350/1240	2.0/20.1	glass, Low-Ca px: $Wo_5En_{80}Fs_{15}$
2012-37	AN-31	1.2	1350/1240	2.0/20.0	glass, Low-Ca px: $Wo_6En_{79}Fs_{15}$
2012-36	MORB	1	1350/1240	2.0/20.1	glass, High-Ca px: $Wo_{29}En_{59}Fs_{12}$, plag:An_{61}
2012-38	MORB	1.2	1350/1240	2.0/20.0	glass, High-Ca px:$Wo_{34}En_{54}Fs_{12}$

Table DR2. Experimental conditions for sulfur partitioning experiments. High and low temperature steps of the experiments are reported, along with the duration of the experiment at the high and at the low temperature steps. Average compositions of phases are given in terms of the wollastonite, enstatite and ferrosilite components of the pyroxenes, in terms of the forsterite component for the olivine and the anorthite component for the plagioclase.

Sulfur analyses

Sulfur in the crystals was measured by two techniques: one experiment was measured on the CAMECA IMS 1280 ion microprobe at the Northeast National Ion Microprobe Facility at Woods Hole Oceanographic Institute, and all experiments were analyzed by synchrotron X-ray fluorescence microprobe (SXRF) on beamline I18 at the Diamond synchrotron (Mosselmans et al, 2009).

The ion microprobe was operated following the techniques described in Dalou et al. (2012) with a Cs^+ primary beam of 1.5 nA current; an electron gun was used to minimize surface charging. The mass resolution used was 5905, which allowed measurement of ^{12}C, ^{19}F, ^{30}Si, ^{32}S and ^{35}Cl; ten cycles were acquired for each mass and then averaged. A 30 × 30 μm raster was used to clean the sample surface and an 18 × 18 μm aperture was applied to analyze the center of the rastered area. Standards used were natural and synthetic glasses (Dalou et al., 2012) and the sulfur concentration determined by the ratio of ^{32}S to ^{30}Si.

SXRF analyses were performed in a helium atmosphere using a 3 keV beam focused to 6×6 μm by a pair of Kirkpatrick-Baez mirrors, and the fluorescence spectra of the samples measured with a Vortex silicon drift detector. S concentrations were determined from the spectra by PyMca (Solé et al., 2007) using the silicon concentration of the minerals as the internal reference for quantification. The accuracy and precision of the analyses were tested by analysis of 4 in-house standard glasses whose S concentrations had been determined by electron microprobe and an orthopyroxene in experiment DRB2012-29 analyzed by ion microprobe. The concentration of the various glasses ranged from 70 to 142 ppm and SXRF analyses were always within 1-sigma standard deviation of the electron microprobe analyses; the average difference between the two methods was 10%. Using these standards we calculate a limit of detection of 1 ppm by two different methods (Rousseau, 2001; Goldstein et al., 2003). Based upon a relative uncertainly of 10% in our electron microprobe analyses as well as 10% uncertainty seen in our peak fitting areas we calculate through error propagation (Rousseau, 2001) an analytical uncertainty of 14% relative for samples with 6 ppm and greater. At 1.6 ppm the uncertainty in the peak fitting areas reaches 37% and the analytical uncertainty becomes 38% relative.

One orthopyroxene crystal from experiment DRB2011-29 was analyzed 6 times by ion microprobe and had an average concentration of 0.69 ± 0.53 (1 sigma standard deviation) ppm S, whereas two analyses of the same orthopyroxene by SXRF yielded a concentration of 2.9 ± 1.8 ppm (individual analyses yielded 4.2 and 1.6 ppm). The similarity of these concentrations suggest that both analytical techniques provide consistent results to within approximately 2 ppm, even near the calculated minimum detection limit of the SXRF.

Experimental results

All experiments produced euhedral to subhedral crystals (Fig. DR1). In all experiments the amount of melt present during crystal growth was greater than 50%. The totals for the analyses of the glasses are all slightly low because of small amounts of water in the starting rock compositions (Table DR3). The low-calcium pyroxenes formed in experiment DRB2012-29 using the AN31 composition fall into the bronzite compositional field and contained 0.64 ± 0.46 ppm S, as measured by the ion microprobe, or 2.9 ± 1.8 ppm, measured by SXRF, and produced an orthopyroxene/melt K_D of either 0.001 (ion microprobe results) or 0.003 (SXRF). Because the S concentration of the orthopyroxene in this sample is so close to the detection limit of the SXRF, the ion microprobe results are preferred. At higher pressures of 1.0 and 1.2 GPa in experiments DRB2012-35 and -37 using the AN31 composition the low-calcium pyroxenes appear to be pigeonitic; these crystals contained 29 ± 9 (SIMS) and 31 ± 9 (SXRF) ppm S (Table DR3), producing pyroxene/melt K_Ds of 0.026 and 0.028, respectively. The sulfur concentrations in the augites crystallized from experiments DRB2012-36 (Fig. DR1) and -38 with the MORB composition have sulfur concentrations that overlap at the 1-sigma level, 29 ± 7 (SIMS) and 25 ± 11 (SXRF) ppm, respectively (Table DR3). These experiments yield sulfur clinopyroxene/melt K_D s of 0.028 and 0.023. The experiments yield very similar K_Ds between clinopyroxene and melt; combining the results for the low-calcium pyroxenes in DRB2012-35 and -37 with those of the augites in DRB20212-36 and -39 produces an average K_D of 0.026 ± 0.009. The uncertainty in all calculated partition coefficients is dominated by the standard deviations of the sulfur analyses in the crystals, but in general the pyroxene/melt K_Ds are accurate to within ~33% relative.

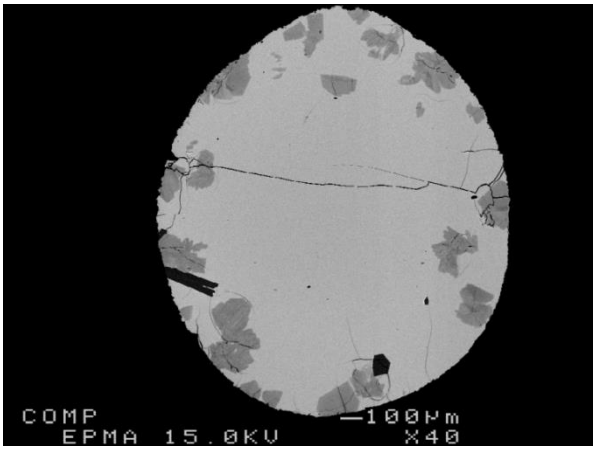

Figure DR1. Backscattered electron image of the experiment DRB2012-36. Euhedral clinopyroxene (dark gray) and plagioclase (black) phenocrysts are scattered in a (light gray) glass.

	2012-29		2012-35		2012-37		2012-36		2012-38	
	mean glass (n = 19)	s.d.	mean glass (n = 12)	s.d.	mean glass (n = 12)	s.d.	mean glass (n = 12)	s.d.	mean glass (n = 12)	s.d.
SiO_2	50.83	0.48	48.85	0.24	49.10	0.23	48.98	0.30	49.33	0.14
TiO_2	1.29	0.07	1.52	0.03	1.40	0.04	1.48	0.11	1.53	0.05
Al_2O_3	13.28	0.16	14.21	0.10	14.14	0.10	16.48	0.12	17.21	0.11
FeO*	10.40	0.21	10.84	0.12	11.11	0.12	10.71	0.23	10.54	0.12
MnO	0.18	0.05	0.18	0.03	0.17	0.04	0.19	0.02	0.17	0.03
MgO	8.80	0.13	8.04	0.07	7.92	0.08	7.18	0.09	6.42	0.06
CaO	10.50	0.18	10.35	0.05	10.09	0.06	10.38	0.07	9.80	0.05
Na_2O	1.98	0.05	2.25	0.04	2.28	0.03	2.92	0.06	3.13	0.02
K_2O	0.81	0.03	0.91	0.02	0.94	0.02	0.13	0.01	0.13	0.01
P_2O_5	0.15	0.02	0.15	0.07	0.16	0.08	0.12	0.07	0.16	0.05
S (ppm)	933	28	1116	22	1096	19	1032	84	1090	27
Total	98.49		97.63		97.63		98.84		98.70	
	pyroxene (n = 9)		**pyroxene (n = 6)**		**pyroxene (n = 8)**		**pyroxene (n = 8)**		**pyroxene (n = 8)**	
	mean	**s.d.**	**mean**	**s.d.**	**mean**	**s.d.**	**mean**	**s.d.**	**mean**	**s.d.**
S (ppm)	0.64	0.46	29	9	31	9	29	7	25	11
K_D	0.001		**0.026**		**0.028**		**0.028**		**0.023**	

Table DR3. Experimental results include major element compositions of the glasses, sulfur concentrations for glasses and pyroxenes and calculated K_Ds. Total iron as FeO. Standard deviation (s.d.) is at 1σ about the mean of the analyses.

TEM analyses

Transmission Electron Microscopy (TEM) observations on the studied samples confirm that the pyroxene crystals are homogeneous and do not contain inclusions, thus excluding the possible occurrence of "hidden" S-bearing nanophases.

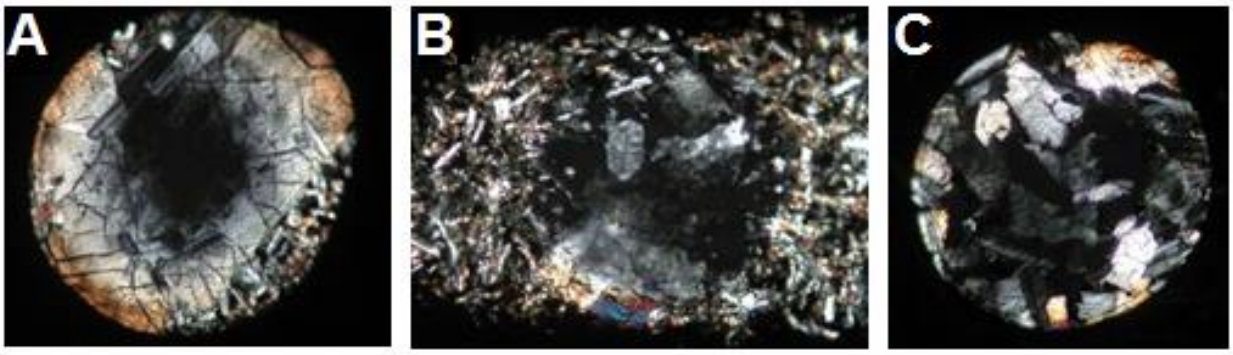

Figure DR2. Three ultra-thin TEM specimens prepared by means of ion milling with DuoMill and PIPS Ion-thinned samples; grid hole diameter of 600 μm (polarizing microscope crossed nicols images) from sample AN510 (A-B; two clinopyroxene phenocrysts) and AN505 (C; several clinopyroxene crystals along with plagioclase and groundmass).

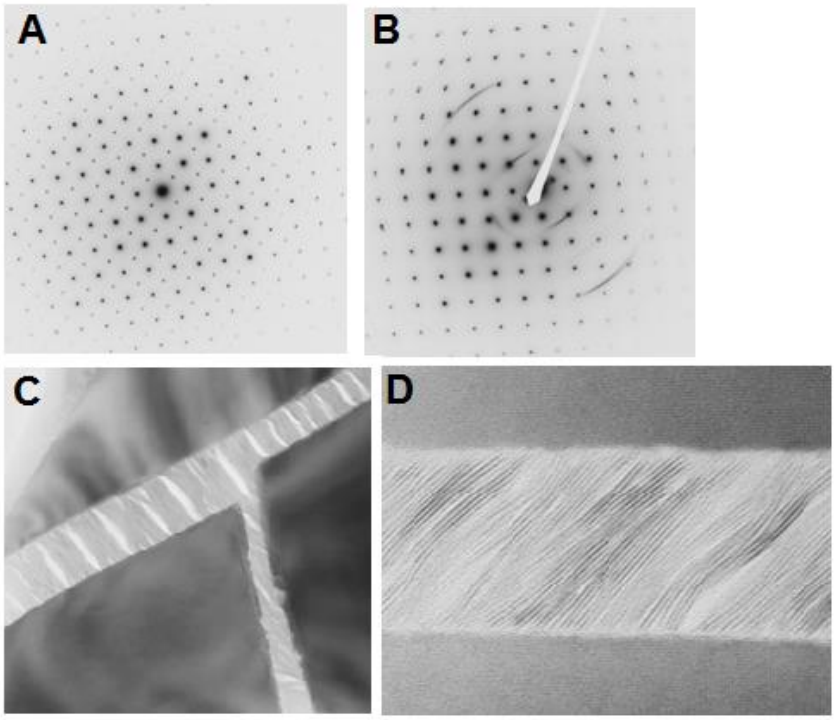

Figure DR3. Selected Area Electron Diffraction patterns reveal sharp and intense reflections (A; a*b* pattern of homogeneous pyroxene single-crystal). Crystal homogeneity is interrupted only by rare alteration veins, filled with poorly crystalline smectite-like material, producing weak and diffuse diffraction "arcs" (B). The thickness of alteration veins is variable (C) and, in high-resolution images, the smectite-like material shows typical wavy and irregular lattice fringes (D; 001).

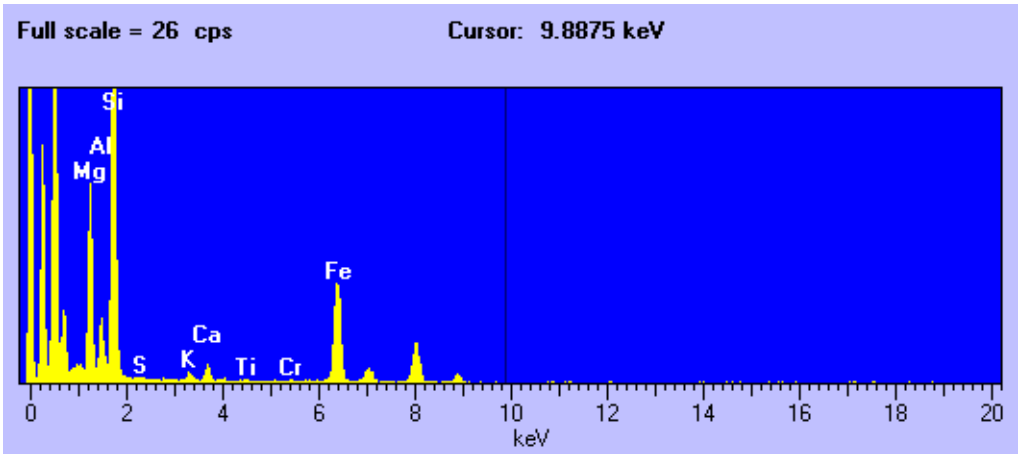

Figure DR4. Representative EDS/TEM spectrum of the Mg and Fe-rich smectite-like material within late alteration veins, obtained by large incident spot to avoid beam damage.

Table DR4a.

Sample		Clinopyroxenes (SXRF)					Calculated equilibrium melt	Clinopyroxene composition (EMPA)										crystallization pressure
LIP	ID	crystal	analyzed spots	S		absolute uncertainty	S	SiO_2	TiO_2	Al_2O_3	FeO_t	MnO	MgO	CaO	Na_2O	Cr_2O_3	Mg#	(Putirka, 2008)
			#	ppm		ppm	ppm	wt.%	wt.%	wt.%	wt.%	wt.%	wt.%	wt.%	wt.%	wt.%		kbar
CAMP	AN134	cpx1	2	6	±	1	212	52.45	0.63	2.63	7.71	0.19	17.30	18.98	0.21	0.51	82	6.5
CAMP	AN134	cpx1	2	20	±	3	769	52.45	0.63	2.63	7.71	0.19	17.30	18.98	0.21	0.51	82	6.5
CAMP	AN134	cpx1	28	14	±	2	529	52.45	0.63	2.63	7.71	0.19	17.30	18.98	0.21	0.51	82	6.9
CAMP	AN134	cpx2	4	26	±	4	1000	53.69	0.48	1.33	8.86	0.28	17.89	17.97	0.14	0.19	81	4.4
CAMP	AN134	cpx2	9	14	±	2	538	52.95	0.48	2.46	7.14	0.18	16.78	19.79	0.16	0.96	83	6.5
CAMP	AN504	cpx3	2	14	±	2	538	52.26	0.69	1.93	9.07	0.27	16.75	18.91	0.17	0.17	79	5.8
CAMP	AN504	cpx4	1	6	±	1	231	52.93	0.37	1.81	9.29	0.22	16.85	18.01	0.21	0.47	79	6.9
CAMP	AN510	cpx1	2	29	±	4	1115	52.67	0.38	2.56	6.09	0.17	17.31	20.15	0.14	1.27	86	4.1
CAMP	AN510	cpx1	2	50	±	7	1904	52.95	0.31	2.31	6.97	0.13	18.12	18.70	0.16	0.95	85	4.5
CAMP	AN510	cpx3	2	36	±	5	1385	52.82	0.35	2.24	6.85	0.15	17.73	19.10	0.17	0.95	84	4.8
CAMP	AN22	cpx1	1	12	±	2	462	53.11	0.26	1.87	6.70	0.18	19.57	18.32	0.16	0.31	86	3.5
CAMP	AN22	cpx1	6	17	±	2	667	52.20	0.34	2.60	6.10	0.17	18.13	19.87	0.18	0.39	86	4.7
CAMP	AN141	cpx2	2	46	±	6	1769	52.64	0.39	3.05	5.86	0.18	17.35	20.76	0.17	0.80	86	4.9
CAMP	AN141	cpx2	2	24	±	3	904	52.85	0.37	3.00	5.86	0.14	17.60	20.23	0.18	0.83	86	5.6
CAMP	AN141	cpx2	18	19	±	3	746	52.84	0.33	2.76	5.67	0.14	17.32	20.09	0.27	0.75	87	8.3
CAMP	AN141	cpx1	2	25	±	3	942	52.72	0.34	3.00	5.28	0.12	17.30	20.49	0.15	1.04	87	5.4
CAMP	AN141	cpx1	19	14	±	2	530	52.85	0.30	2.60	7.07	0.17	19.41	18.00	0.15	0.47	85	5.2
CAMP	AN730	cpx1	2	26	±	4	981	52.38	0.38	1.76	9.19	0.27	17.71	17.87	0.19	0.05	80	5.9
CAMP	AN730	cpx2	2	33	±	5	1250	52.24	0.29	1.91	7.15	0.19	18.38	19.00	0.20	0.25	84	4.4
CAMP	AN156A	cpx1	2	16	±	2	615	52.38	0.36	1.73	10.73	0.26	16.44	17.53	0.23	0.19	76	7.0
CAMP	AN156A	cpx1	2	10	±	1	365	52.38	0.36	1.73	10.73	0.26	16.44	17.53	0.23	0.19	76	7.4
CAMP	NEW31	cpx1	4	14	±	2	548	51.90	0.29	2.71	7.07	0.14	19.59	16.48	0.29	0.57	85	11.4
CAMP	NEW31	cpx1	18	5	±	1	190	51.90	0.29	2.71	7.07	0.14	19.59	16.48	0.29	0.57	85	11.8
CAMP	CS31	cpx1	1	13	±	2	500	52.42	0.11	2.05	9.13	0.25	17.66	17.73	0.24	0.40	80	12.3
CAMP	CS62	cpx2	2	23	±	3	885	49.69	0.62	4.38	9.66	0.23	14.79	19.72	0.35	0.27	76	14.7
CAMP	CS62	cpx3	2	20	±	3	750	49.69	0.62	4.38	9.66	0.23	14.79	19.72	0.35	0.27	76	15.1
CAMP	SIN23	cpx2	1	12	±	2	462	50.05	0.96	3.20	9.43	0.20	16.11	19.14	0.30	0.38	78	9.1
CAMP	SIN23	cpx2	1	13	±	2	500	50.13	1.04	3.17	9.45	0.23	15.95	19.13	0.30	0.39	78	10.0
CAMP	SIN23	cpx1	2	16	±	2	615	50.38	1.06	2.15	13.27	0.29	15.74	17.20	0.30	0.00	71	
CAMP	M13	cpx1	2	3	±	1	96	50.43	0.80	2.56	10.30	0.24	15.66	18.97	0.26	0.18	76	9.6
CAMP	M13	cpx2	2	2	±	0.4	58	50.78	0.71	1.95	11.30	0.28	15.80	18.38	0.30	0.04	75	
Paranà-Etendeka	SALT280	cpx1	2	4	±	1	154	50.89	0.94	1.20	14.41	0.41	16.08	15.50	0.20	0.04	70	21.4
Paranà-Etendeka	SALT280	cpx2	2	7	±	1	250	50.44	1.18	1.72	12.11	0.27	15.09	18.51	0.26	0.03	72	23.0
Paranà-Etendeka	SALT280	cpx1	2	3	±	1	96	50.44	1.18	1.72	12.11	0.27	15.09	18.51	0.26	0.03	72	22.6
Paranà-Etendeka	SALT280	cpx1	2	5	±	1	173	50.24	1.11	1.76	12.11	0.29	15.30	18.67	0.26	0.03	73	23.8
Paranà-Etendeka	9020	cpx1	5	14	±	2	546	51.16	0.86	1.72	12.08	0.25	15.36	18.25	0.27	0.02	73	26.2
Paranà-Etendeka	9020	cpx1a	2	19	±	3	731	50.65	1.16	2.21	10.42	0.22	15.41	19.28	0.27	0.04	76	26.0
Paranà-Etendeka	2071	cpx1	2	5	±	1	192	50.78	1.09	1.81	13.72	0.32	14.78	17.20	0.21	0.01	69	25.2
Paranà-Etendeka	2071	cpx2	1	5	±	1	192	50.78	1.09	1.81	13.72	0.32	14.78	17.20	0.21	0.01	69	14.0
Paranà-Etendeka	B168	cpx1	2	3	±	1	96	51.42	0.93	1.49	13.16	0.49	16.69	16.08	0.17	0.00	73	11.3
Paranà-Etendeka	B168	cpx1	2	3	±	1	115	50.75	1.10	2.05	12.52	0.29	14.49	18.55	0.23	0.03	71	11.6
Paranà-Etendeka	B168	cpx2	3	8	±	1	321	50.37	1.14	2.16	13.29	0.35	14.79	17.22	0.23	0.01	70	11.2
Paranà-Etendeka	UR54	cpx4	1	13	±	2	500	51.44	0.51	1.89	12.20	0.32	15.80	17.06	0.24	0.11	73	15.6
Paranà-Etendeka	UR54	cpx4	2	16	±	2	615	51.44	0.51	1.89	12.20	0.32	15.80	17.06	0.24	0.11	73	16.4
Paranà-Etendeka	UR54	cpx2	1	6	±	1	231	51.87	0.44	1.81	10.74	0.32	17.70	16.42	0.15	0.07	78	15.9
Paranà-Etendeka	UR59	cpx1	2	7	±	1	269	52.15	0.34	1.88	7.91	0.23	18.27	18.36	0.16	0.18	83	14.9
Paranà-Etendeka	UR59	cpx1	2	6	±	1	212	52.15	0.34	1.88	7.91	0.23	18.27	18.36	0.16	0.18	83	14.5
Paranà-Etendeka	UR59	cpx3	1	6	±	1	231	51.86	0.43	1.81	9.80	0.31	17.30	18.06	0.17	0.11	79	13.4
Paranà-Etendeka	UR81	cpx3	1	3	±	1	115	52.66	0.38	1.17	8.37	0.30	19.05	17.66	0.16	0.18	83	18.1
Paranà-Etendeka	UR81	cpx3	15	9	±	1	364	52.66	0.38	1.17	8.37	0.30	19.05	17.66	0.16	0.18	83	18.3
Paranà-Etendeka	UR81	cpx3	16	7	±	1	269	52.66	0.38	1.17	8.37	0.30	19.05	17.66	0.16	0.18	83	17.3
Paranà-Etendeka	UR81	cpx1	18	5	±	1	182	50.15	0.51	2.40	6.99	0.21	17.60	19.55	0.18	0.60	84	17.7
Paranà-Etendeka	B189	cpx1	6	13	±	2	513	50.64	0.70	3.93	8.09	0.15	15.73	20.00	0.27	0.38	80	11.7
Paranà-Etendeka	B189	cpx1a	6	18	±	3	699	50.64	0.70	3.93	8.09	0.15	15.73	20.00	0.27	0.38	80	9.8
Deccan Traps	D242	cpx1	1	10	±	1	385	51.79	0.72	2.38	7.50	0.20	17.12	19.22	0.24	0.42	83	12.7
Deccan Traps	D242	cpx1	1	19	±	3	731	51.79	0.72	2.38	7.50	0.20	17.12	19.22	0.24	0.42	83	12.8
Deccan Traps	D242	cpx3	1	20	±	3	769	50.83	0.79	2.76	7.62	0.12	16.88	19.62	0.25	0.58	82	13.5
Deccan Traps	D242	cpx3a	1	8	±	1	308	50.83	0.79	2.76	7.62	0.12	16.88	19.62	0.25	0.58	82	14.0
Deccan Traps	D242	cpx3a	26	24	±	3	938	50.83	0.79	2.76	7.62	0.12	16.88	19.62	0.25	0.58	82	14.3
Deccan Traps	D242	cpx3	24	49	±	7	1869	50.83	0.79	2.76	7.62	0.12	16.88	19.62	0.25	0.58	82	14.2
Deccan Traps	D244	cpx1	4	9	±	1	346	51.66	0.92	2.36	9.06	0.25	16.36	19.24	0.25	0.52	79	12.3
Deccan Traps	D244	cpx1	4	10	±	1	365	51.66	0.92	2.36	9.06	0.25	16.36	19.24	0.25	0.52	79	12.6
Deccan Traps	D244	cpx1b	4	10	±	1	365	51.66	0.92	2.36	9.06	0.25	16.36	19.24	0.25	0.52	79	13.0
Deccan Traps	D244	cpx1c	4	4	±	1	154	51.66	0.92	2.36	9.06	0.25	16.36	19.24	0.25	0.52	79	14.2

Table DR4b.

Sample		Whole rock composition (XRF)													
LIP	**rock**	**SiO_2 wt.%**	**TiO_2 wt.%**	**Al_2O_3 wt.%**	**FeO_t wt.%**	**MnO wt.%**	**MgO wt.%**	**CaO wt.%**	**Na_2O wt.%**	**K_2O wt.%**	**P_2O_5 wt.%**	**TOT wt.%**	**Mg# (0.15)**	**Zr ppm**	**Y ppm**
CAMP	AN134	53.67	1.43	14.28	9.92	0.18	7.25	9.97	2.15	0.98	0.17	100.0	60	147	26
CAMP	AN504	53.48	1.54	13.93	9.74	0.16	8.25	9.83	2.23	0.64	0.19	100.0	64	124	28
CAMP	AN510	53.76	1.36	13.92	10.77	0.17	7.03	10.20	2.03	0.60	0.16	100.0	58	118	29
CAMP	AN22	52.05	1.06	15.26	9.08	0.17	8.09	11.96	1.94	0.28	0.11	100.0	65	76	20
CAMP	AN141	52.14	1.04	14.87	9.97	0.18	7.74	11.45	1.90	0.59	0.11	100.0	61	78	20
CAMP	AN730	53.52	1.21	14.27	11.01	0.18	6.43	10.21	2.42	0.74	0.14	100.0	54	97	25
CAMP	AN156A	51.44	1.63	13.63	14.04	0.22	5.94	10.44	2.14	0.35	0.17	100.0	46	115	41
CAMP	NEW31	52.64	1.13	14.24	10.31	0.17	7.92	11.24	2.04	0.32	0.15	100.0	61	97	22
CAMP	CS31	49.93	0.61	15.53	9.78	0.17	10.46	11.20	1.96	0.35	0.09	100.0	69	50	22
CAMP	CS62	48.56	0.67	16.80	10.85	0.18	9.39	11.17	2.10	0.28	0.11	100.0	64	38	24
CAMP	SIN23	49.03	2.91	13.72	14.15	0.21	6.64	10.38	2.23	0.42	0.30	100.0	50	183	36
CAMP	M13	49.63	2.13	14.41	13.27	0.28	7.23	10.17	2.37	0.29	0.16	100.0	53	110	20
Paranà-Etendeka	SALT280	51.15	3.49	13.47	13.58	0.21	4.65	8.79	2.66	1.51	0.48	100.0	42	246	36
Paranà-Etendeka	9020	51.80	4.14	13.40	12.45	0.16	4.70	7.95	2.53	1.97	0.90	100.0	44	293	37
Paranà-Etendeka	2071	52.33	3.44	13.93	12.95	0.20	3.91	8.23	2.81	1.61	0.59	100.0	39	263	39
Paranà-Etendeka	B168	50.79	4.29	13.62	14.03	0.19	3.39	9.22	2.92	0.94	0.61	100.0	34	237	26
Paranà-Etendeka	UR54	56.82	1.26	14.36	10.06	0.17	4.59	8.58	2.47	1.49	0.20	100.0	49	129	26
Paranà-Etendeka	UR59	52.67	1.14	15.74	9.52	0.17	5.98	10.96	2.54	1.13	0.14	100.0	57	157	30
Paranà-Etendeka	UR81	49.48	1.42	19.03	10.08	0.15	7.49	8.88	1.91	1.15	0.41	100.0	61	135	29
Paranà-Etendeka	B189	50.57	1.80	15.75	12.31	0.18	5.29	10.81	2.39	0.64	0.26	100.0	47	126	20
Deccan Traps	D242	50.72	2.47	14.33	11.44	0.20	6.97	10.82	2.40	0.29	0.36	100.0	56	-	-
Deccan Traps	D244	51.80	3.16	13.78	12.28	0.21	5.05	10.05	2.89	0.35	0.44	100.0	46	-	-

Table DR4c.

Sample details						Sample coordinates				
LIP	**ID**					**Latitude**		**Longitude**		**Locality**
CAMP	AN134	Morocco, Central High Atlas	low Ti	Lower Unit	flow	31° 07' 74"	N	7° 22' 70"	W	Tiourjdal
CAMP	AN504	Morocco, Meseta	low Ti	Lower Unit	flow	32° 38' 57.4"	N	5° 24' 28.8"	W	Maaziz
CAMP	AN510	Morocco, Meseta	low Ti	Intermediate Unit	flow	32° 38' 57.4"	N	5° 24' 28.8"	W	Maaziz
CAMP	AN22	Morocco, Central High Atlas	low Ti	Upper Unit	flow	31° 32' 50"	N	7° 40' 20"	W	Aït Ourir
CAMP	AN141	Morocco, Central High Atlas	low Ti	Upper Unit	flow	31° 07' 74"	N	7° 22' 70"	W	Tiourjdal
CAMP	AN730	Morocco, Anti Atlas	low Ti	Upper Unit	sill	29° 51' 27.6"	N	7° 15' 58.2"	W	Tissint
CAMP	AN156A	Morocco, Central High Atlas	low Ti	Recurrent Unit	flow	31° 10' 44"	N	7° 29' 82"	W	Tazgaoute
CAMP	NEW31	U.S.A., Virginia, Culpeper Basin	low Ti	Orange Mt.	flow	40° 52' 47.1"	N	74° 11' 11.7"	W	Clifton UBC Quarry
CAMP	CS31	U.S.A., South Carolina	low Ti		dyke	34° 44' 21.3"	N	80° 35' 0.0"	W	Tradesville
CAMP	CS62	U.S.A., North Carolina	low Ti		dyke	36° 09' 26.7"	N	80° 23' 40.1"	W	Chesterfield
CAMP	SIN23	Guyana	high Ti		dyke	4° 49' 55.79"	N	52° 56' 23"	W	Montagnes Bois-Violets
CAMP	M13	Brazil, Maranhão Basin	high Ti		flow	7° 11' 35"	S	48° 14' 07"	W	Araguaina
Paranà-Etendeka	SALT280	Uruguay	high Ti	Pitanga formation	flow	31° 23' 00"	S	57° 57' 00"	W	Salto
Paranà-Etendeka	9020	Brazil	high Ti	Espinacho	dyke	19° 41' 43.6"	S	43° 04' 13.2"	W	Nova Era
Paranà-Etendeka	2071	Brazil	high Ti	Pitanga formation	flow	23° 14' 2.40"	S	49° 19' 58.8"	W	Ourinhos
Paranà-Etendeka	B168	Brazil	high Ti	Parapanema formation	flow	20° 18' 46.8"	S	47° 48' 7.2"	W	Uberaba
Paranà-Etendeka	UR54	Uruguay	low Ti	Gramado formation	dyke	32° 15' 55.28"	S	55° 01' 43.48"	W	Ansina- Tacuarembò
Paranà-Etendeka	UR59	Uruguay	low Ti	Gramado formation	dyke	32° 52' 41.79"	S	55° 37' 21.91"	W	Blanquillo
Paranà-Etendeka	UR81	Uruguay	low Ti	Esmeralda formation	flow	30° 25' 27.39"	S	56° 27' 6.82"	W	Artigas
Paranà-Etendeka	B189	Brazil	low Ti	Ribeira formation	flow	20° 11' 9.6"	S	50° 39' 53.2"	W	Jales
Deccan Traps	D242	India	high Ti	Mahabaleshwar unit	flow	17° 56' 32.13"	N	73° 52' 06.84"	E	Wai
Deccan Traps	D244	India	high Ti	Mahabaleshwar unit	flow	17° 56' 07.29"	N	73° 33' 48.81"	E	Mahabaleshwar

Table DR4 a-c. Sulfur concentrations in the clinopyroxene and those calculated for the equilibrium melt are displayed (a). Reported are also major element compositions (EMPA) for the analyzed augites (a) and major element (XRF) and Zr and Y (ICPMS) compositions for the relative whole rocks (b). Coordinates of the sampling sites are also included (c).

Mineral chemistry on pyroxenes was investigated with a CAMECA SX50 electron microprobe at the IGG-CNR of Padova, at 20 nA beam current, 20 kV acceleration voltage, 10-20 seconds counting time for the peak and 5-10 seconds for high and low backgrounds. Uncertainties on the data are 1% for major elements. The 42 clinopyroxenes from these three LIPs ($Wo_{32-44}En_{42-55}Fs_{9-23}$), have non quadrilateral components ranging between 1 and 8% (aegirine up to 4.6 and jadeite up to 4.5%).

Most of the clinopyroxenes analyzed for S in this study are in equilibrium with their host rocks based upon Fe-Mg partitioning. This equilibrium supports the use of sulfur partition coefficients to calculate magmatic sulfur concentrations. The Fe^{2+} in the clinopyroxenes was calculated from Fe_{tot} after Papike et al. (1974) and a partition coefficient of 0.25±0.05 (Gaetani and Grove, 1998) was applied. Most samples contained augitic phenocrysts in equilibrium with the host whole-rock, demonstrating that the analyzed augites are not xenocrysts and that open-system magmatic processes (e.g. magma mixing), that can lead to non-equilibrium conditions unsuitable for the application of the clinopyroxene/melt sulfur K_D, were not dominant. The equilibrium between the clinopyroxenes and their host rocks supports application of the clinopyroxene/melt K_D based technique to estimate magmatic sulfur concentrations.

REFERENCES CITED

Baker, D.R., 2004, Piston cylinder calibration at 400 to 500 MPa: a comparison of using water solubility in albite melt and NaCl melting: American Mineralogist, v. 89, p. 1553-1556, doi: 0003-004X/04/0010–1553$05.00.

Dalou, C., Koga, K.T., Shimizu, N., Boulon, J., and Devidal, J.-L., 2012, Experimental determination of F and Cl partitioning between lherzolite and basaltic melt: Contributions to Mineralogy and Petrology, v. 163, p. 591-609, doi: 10.1007/s00410-011-0688-2.

Gaetani, G.A., and Grove, T.L., 1998, The influence of water on melting of mantle peridotite: Contributions to Mineralogy and Petrology, v. 131, p. 323-346, doi: 10.1007/s004100050396.

Goldstein, J., Newbury, D.E., Joy, D.C., Lyman, C.E., Echlin, P., Lifshin, E., Sawyer, L., Michael, J.R., 2003, Scanning Electron Microscopy and X-ray Microanalysis, Springer-Verlag, New York, ed. 3, 690 p.

Jugo, P.J., Wilke, M., and Botcharnikov, R.E., 2010, Sulfur K-edge XANES analysis of natural and synthetic basaltic glasses: Implications for S speciation and S content as function of oxygen fugacity: Geochimica et Cosmochimica Acta, v. 74, no. 20, p. 5926–5938, doi: 10.1016/j.gca.2010.07.022.

Liu, Y., Samaha, N.-T., and Baker, D.R., 2007, Sulfur concentration at sulfide saturation (SCSS) in magmatic silicate melts: Geochimica et Cosmochimica Acta, v. 71, no. 7, p. 1783–1799, doi: 10.1016/j.gca.2007.01.004.

Mosselmans, J.F.W., Quinn, P.D., Dent, A.J., Cavill, S.A., Moreno, S.D., Peach, A., Leicester, P.J., Keylock, S.J., Atkinson, K.D., Rosell, J.R., Gregory, S.R., 2009, I18 – the microfocus spectroscopy beamline at the Diamond Light Source: Journal of Synchrotron Radiation, v. 16, no. 6, p. 818-824, doi: 10.1107/S0909049509032282.

Papike, J.J., Cameron, K.L. and Baldwin, K., 1974, Amphiboles and pyroxenes: characterization of other than quadrilateral components and estimates of ferric iron from microprobe data: Geological Society of America Abstracts with Programs, v. 6, p. 1053-1054.

Putirka, K., 2008, Thermometers and Barometers for Volcanic Systems, in: Putirka, K., and Tepley, F., Eds., Minerals, Inclusions and Volcanic Processes, Reviews in Mineralogy and Geochemistry, Mineralogical Soc. Am., Volume 69, p. 61-120, doi: 10.2138/rmg.2008.69.3.

Rousseau, R.M., 2001, Detection limit and estimate of uncertainty of analytical XRF results: The Rigaku Journal, v. 18, p. 33-47.

Solé, V.A., Papillon, E., Cotte, M., Walter, P., and Susini, J., 2007, A multiplatform code for the analysis of energy-dispersive X-ray fluorescence spectra: Spectrochimica Acta Part B: Atomic Spectroscopy, v. 62, no. 1, p. 63–68, doi: 10.1016/j.sab.2006.12.002.